PNAS RESEARCH ARTICLE | BIOPHYSICS AND COMPUTATIONAL BIOLOGY

Indentation induces instantaneous nuclear stiffening and unfolding of nuclear envelop wrinkles

Wentian Tang[a], Xin Chen[b,c], Xian Wang[a,b], Min Zhu[c], Guanqiao Shan[a], Tiancong Wang[a], Wenkun Dou[a], Jintian Wang[a], Junhui Law[a], Zheyuan Gong[a], Sevan Hopyan[c,d,e,1,2], Xi Huang[b,c,d,1,2], and Yu Sun[a,f,g,h,1]

Edited by Yonggang Huang, Northwestern University, Evanston, IL; received May 3, 2023; accepted July 21, 2023

The nuclear envelope (NE) separates genomic DNA from the cytoplasm and regulates transport between the cytosol and the nucleus in eukaryotes. Nuclear stiffening enables the cell nucleus to protect itself from extensive deformation, loss of NE integrity, and genome instability. It is known that the reorganization of actin, lamin, and chromatin can contribute to nuclear stiffening. In this work, we show that structural alteration of NE also contributes to instantaneous nuclear stiffening under indentation. In situ mechanical characterization of cell nuclei in intact cells shows that nuclear stiffening and unfolding of NE wrinkles occur simultaneously at the indentation site. A positive correlation between the initial state of NE wrinkles, the unfolding of NE wrinkles, and the stiffening ratio (stiffness fold-change) is found. Additionally, NE wrinkles unfold throughout the nucleus outside the indentation site. Finite element simulation, which involves the purely passive process of structural unfolding, shows that unfolding of NE wrinkles alone can lead to an increase in nuclear stiffness and a reduction in stress and strain levels. Together, these results provide a perspective on how cell nucleus adapts to mechanical stimuli through structural alteration of the NE.

nuclear stiffening | nuclear envelop wrinkles | nuclear mechanics | intracellular measurement | magnetic micromanipulation

Significance

This work demonstrates how cell nucleus responds to mechanical stimuli through structural alteration of the nuclear envelope (NE). Through a combination of in situ mechanical characterization of intact cell nuclei and numerical simulations, we provide insights into the role of NE wrinkles unfolding in instantaneous nuclear stiffening under indentation. Moreover, simulation shows that structural alteration alone, as a passive process, can increase nuclear stiffness and reduce stress and strain levels. These findings suggest that, in response to mechanical stimuli, the cell nucleus undergoes restructuring by unfolding NE wrinkles, which together with other active processes such as the reorganization of actin, lamin, and chromatin contributes to nuclear stiffening.

Emerging evidence shows that the cell nucleus responds to mechanical stimuli by nuclear stiffening, preventing significant deformation that can lead to nuclear envelope (NE) rupture and DNA damage (1, 2). Nuclear stiffening has been shown to occur under hours-long shear force application (3, 4), or low-intensity vibration (5). It can also occur within seconds after applying a compressive force (6) or tensile force (7).

Multiple cellular components contribute to the regulation of nuclear stiffness. The nuclear lamina is a mesh-like network of lamins and lamin-binding membrane proteins, which is anchored to the inner NE (8). As a major structural component of the NE, it provides resistance to nuclear deformation (9). Changes in concentration (10, 11) and mutation (12–15) of its major component, lamins, can alter nuclear stiffness. The cell nucleus was found to stiffen in conjunction with the recruitment of lamins at the nuclear periphery under shear force (3), indicating the contributing role of the nuclear lamina in nuclear stiffening. This was also found when a tensile force was applied to isolated nuclei with chromatin digested by DNase (7). Other cellular components including actin cytoskeleton, the linker of nucleoskeleton and cytoskeleton (LINC) complex, and chromatin also contribute to nuclear stiffening under an applied force (16). When the actin cytoskeleton was disrupted, a significant decrease in nuclear stiffening was observed (6). Although the role of actin in nuclear stiffening is not yet fully understood, studies (17, 18) suggest that the actin cytoskeleton may impact the stiffness of the cell nucleus by regulating the distribution and organization of lamins (19). Depletion of nesprin, which is a component of the LINC complex, was also shown to alter nuclear stiffening (7). Furthermore, heterochromatin accumulates at the nuclear periphery as a means of gene silencing (20) and impacts the mechanical stability of the cell nucleus (21–23). The condensation and decondensation of chromatin are associated with changes in nuclear stiffness (24, 25), and tension (26) and low-intensity vibration (5) can trigger the reorganization of heterochromatin.

The structural characteristics of cellular components also contribute to the regulation of nuclear stiffness and the response of the cell nucleus to forces. For instance, when actin reorganizes and forms an actin cap, it provides resistance to nuclear deformation and protects the nuclear structural integrity under mechanical stimuli (19). Wrinkles are ubiquitous on curved biological surfaces across multiple scales (27). NE wrinkles (Movie S1), are present in the nucleus of a variety of cells, including but not limited to fibroblasts (28, 29), epithelial cells (30, 31), mesenchymal stromal cells (32), and progenitor cells (33). NE wrinkles exhibit a high level of heterogeneity (Fig. 1*A*), which was suggested to

Author contributions: W.T., X.C., X.W., G.S., W.D., J.L., X.H., and Y.S. designed research; W.T., T.W., J.W., and Z.G. performed research; X.C., M.Z., and S.H. contributed new reagents/analytic tools; W.T. and T.W. analyzed data; X.W., M.Z., and J.L. contributed to simulation; and W.T. wrote the paper.

The authors declare no competing interest.

This article is a PNAS Direct Submission.

[1]To whom correspondence may be addressed. Email: sevan.hopyan@sickkids.ca, xi.huang@sickkids.ca, or sun@mie.utoronto.ca.

[2]S.H. and X.H. are co-corresponding authors.

This article contains supporting information online at https://www.pnas.org/lookup/suppl/doi:10.1073/pnas.2307356120/-/DCSupplemental.

Published August 28, 2023.

be associated with differences in cell contractility (30, 33). The shape change of adherent cells, such as from round to flat due to adhesion (28) or from flat to round under the treatment of trypsin (34), was found to be accompanied by a switch between a smooth state and a highly wrinkled state of the NE. Upon spatial confinement, NE wrinkles can unfold (35, 36), significantly changing the curvature of the NE. Inspired by the mathematical relationship between curvature-induced stiffness and geometry of wrinkled sheets (37, 38), and curvature-induced stiffening caused by the bending of a thin sheet (39), we hypothesized that the unfolding of NE wrinkles contributes to nuclear stiffening.

In this study, we conducted in situ mechanical characterization of cell nuclei in intact cells using magnetic tweezers. It was found that the unfolding of NE wrinkles occurred together with instantaneous nuclear stiffening, within seconds of force application directly to the cell nucleus. A quantitative relationship was established between changes of the cell nucleus stiffness and the unfolding of NE wrinkles. Additionally, our observations revealed that the applied forces caused the NE to flatten and smoothen outside the indentation site, impacting the entire cell nucleus rather than only the indentation site. The finite element simulation, which involved the purely passive process of structural unfolding, showed that unfolding of NE wrinkles alone can increase nuclear stiffness and reduce stress and strain levels. These results revealed the role of NE wrinkles in the instantaneous stiffening of the cell nucleus, providing an additional perspective on how the cell nucleus adapts to mechanical stimuli through structural alteration.

Results

In Situ Mechanical Characterization of Cell Nucleus. To measure the mechanical properties of the cell nucleus, a single-pole magnetic tweezers system was developed to apply a force directly on the nucleus through a magnetic bead (diameter: 2.8 μm, Dynabeads M-270 Streptavidin; Invitrogen) inside an intact cell (Fig. 1*B*). The system is capable of generating forces up to 10 nanonewton (nN) with a current of 1 A (*SI Appendix*, Fig. S1) to induce micrometer-scale deformations of the cell nucleus. The magnetic

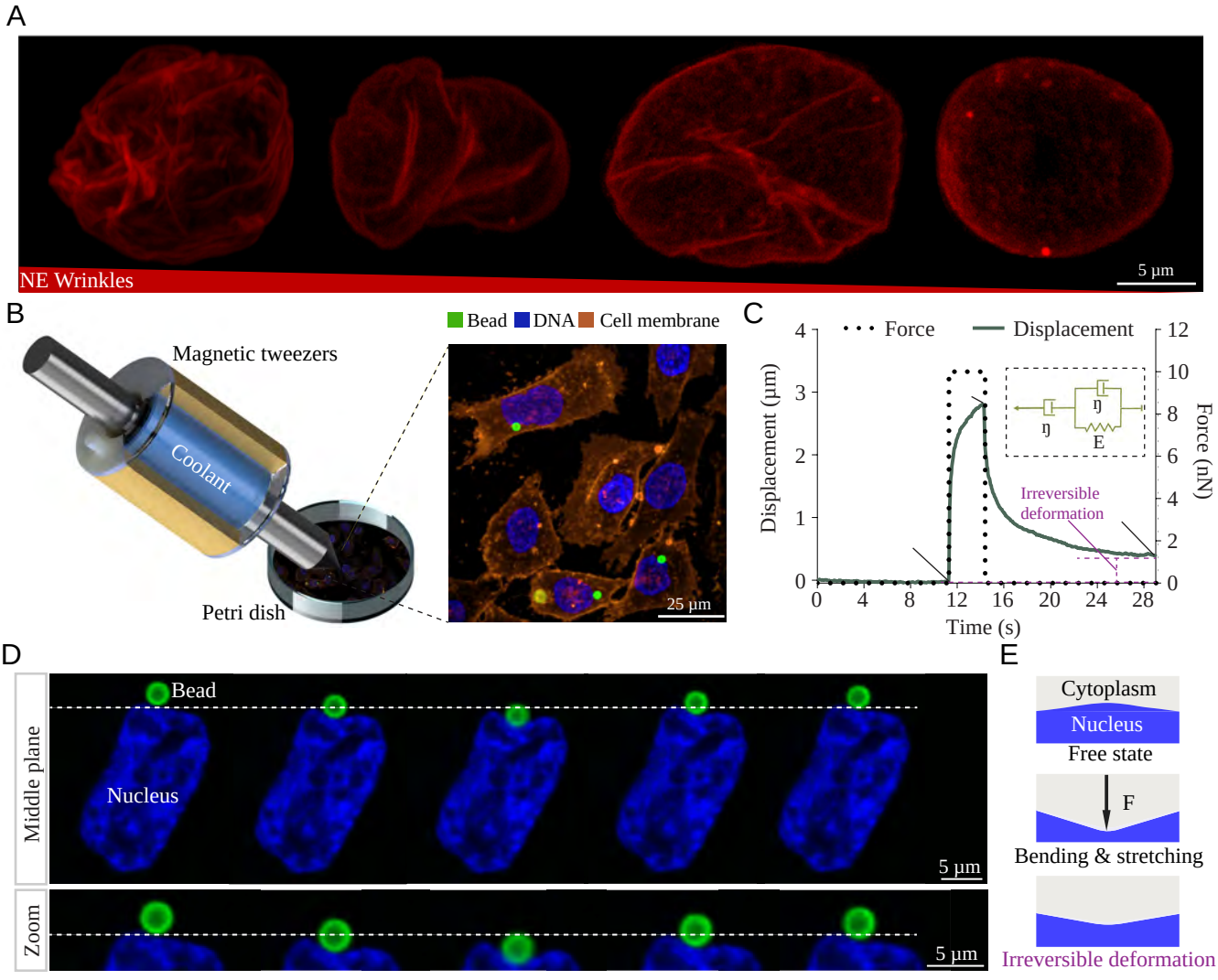

Fig. 1. NE wrinkles and in situ mechanical characterization of cell nucleus. (*A*) Maximum projection confocal z-stack images of cells expressing Lap2 Beta-RFP (a marker of NE). The NE shows a wrinkled or folded morphology (NE wrinkles), which exhibits a high level of heterogeneity. (*B*) Schematic of the single-pole magnetic tweezers. Beads were internalized by cells via endocytosis. Hoechst 33342 and CellMask plasma membrane stain (Invitrogen) were used for the live imaging of DNA and cell membrane. (*C* and *D*) Experimentally measured nuclear deformation over time. A constant force of 10 nN was applied for 3 s and then removed. Both an irreversible deformation (represented by purple dotted line) and an elastic deformation were observed due to an immediate elastic response followed by a viscous flow. Data were interpreted with the anti-Zener viscoelastic model, where η_1 and η_2 represent viscosity and E represents effective elastic modulus. i, ii, and iii denote the three important time points during the measurement process: start, release, and recovery. (*E*) Illustration of the response of the cell nucleus to the applied force. The cell nucleus is bent and stretched and has an irreversible deformation after the force is removed.

beads were functionalized by Atto 488 dye using a streptavidin–biotin binding approach, whereby the biotin-conjugated Atto 488 dye was incorporated onto the surface of the streptavidin-coated magnetic beads (*SI Appendix*, Fig. S2). The beads were internalized by cells via endocytosis after functionalization (*SI Appendix*, Fig. S3). During mechanical measurement, a bead was controlled to apply a constant force of 10 nN on the cell nucleus for 3 s, and then the force was removed (Fig. 1 *C* and *D*). The magnetic force and the measured displacement were fitted into an anti-Zener model, which captures both the elastic and slow viscous behaviors (*SI Appendix*, Fig. S4), to calculate the effective elastic modulus (E) and viscosity (η_1 and η_2) of the cell nucleus. Besides elastic deformation, an irreversible deformation of the cell nucleus (purple dotted line in Fig. 1*C*) was also observed after the force was released, even after 20 times of time constant $\tau = \eta_1/E$ (*SI Appendix*, Fig. S5). The cell nucleus was bent and stretched, and the deformation was irreversible upon the removal of the force, as illustrated in Fig. 1*E*. This behavior was attributed to an initial elastic response, followed by a viscous flow.

Nuclear Stiffening Occurs within Seconds. To monitor the structural alteration of the NE under forces, T24 cells (human bladder carcinoma cell line) were transfected to express Lap2β-RFP for the visualization of NE localization and dynamics under fluorescence microscopy (Fig. 2*A*). Wrinkles are present in both NE and nuclear lamina, suggesting that the observed wrinkled morphology extends across the barrier between the cytoplasm and nucleoplasm (*SI Appendix*, Fig. S6). To investigate nuclear stiffening, a cyclic force was applied via the magnetic bead on the NE, and the stiffness of the same cell nucleus was measured at each force cycle (Fig. 2*B*). In each measured cell, the process of force loading, and NE recovery was repeated five times. The first cycle is referred to as precycle, and the subsequent four cycles are identified as cycles 1 to 4. In each cycle, a constant force of 10 nN was applied for 3 s, followed by 15 s of NE relaxation, which was sufficiently long considering the time constant (0.34 ± 0.17 s). The precycle was performed to ensure full contact between the magnetic bead and the NE. In the subsequent cycles, the displacement of the magnetic bead was measured to represent the deformation of the NE (blue dotted line in Fig. 2*B*).

To show the spatial positions of the magnetic bead and the NE over time, a kymograph was plotted (Fig. 2*C*), and the kymograph line was oriented along the direction of the applied force (*SI Appendix*, Fig. S7), allowing for the visualization of dynamic changes in their positions. Relative deformation and relative effective elastic modulus, which were calculated by normalizing to those measured in cycle 1, were used to quantify the deformation and effective elastic modulus across different cells. The mean relative deformation of each cycle exhibits a statistically significant trend of decrease (cycle 1: 1, cycle 2: 0.94 ± 0.06, cycle 3: 0.88 ± 0.07, cycle 4: 0.85 ± 0.09; posttest for trend, ****$P < 0.0001$), indicating a reduction in the deformability of the NE (Fig. 2*D*). The effective elastic modulus was interpreted from the deformation data of cycles 1 to 4 by fitting into the anti-Zener viscoelastic

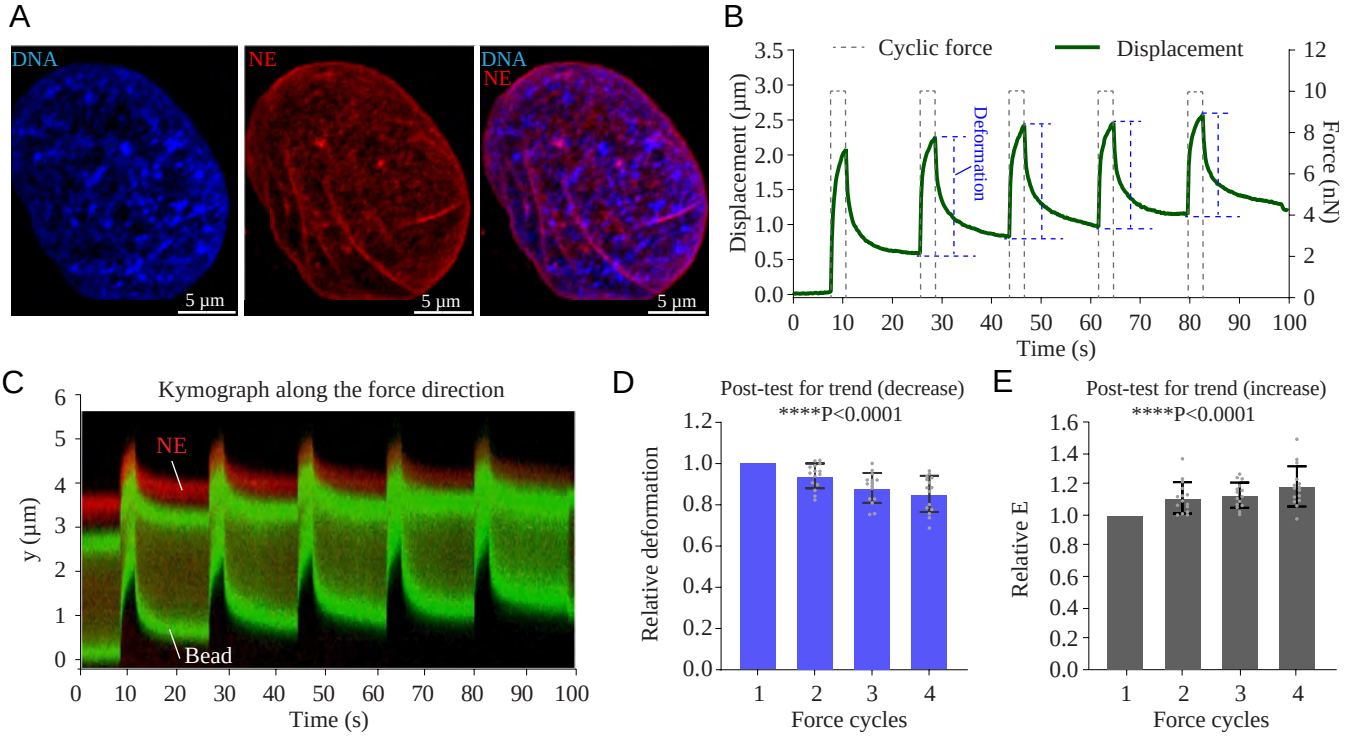

Fig. 2. Nuclear stiffening occurs within seconds. (*A*) Maximum projection confocal z-stack image of a cell expressing Lap2 Beta-RFP that co-stained DNA with Hoechst. Nuclear wrinkles were observed on the NE. (*B*) Magnetic bead displacement during cyclic force application. Each cycle included the application of a constant force of 10 nN for 3 s, followed by 15 s of force release. Force loading and NE recovery were repeated five times in each measured cell. The first cycle is defined as the precycle to ensure full contact between the magnetic bead and the NE. The subsequent four cycles are defined as cycle 1 to cycle 4. NE deformation is indicated by the blue dotted line. (*C*) A kymograph shows the spatial position of the bead and the NE over time. The *X* axis represents time, and the *Y* axis represents the position of the bead and the NE along the force direction. (*D*) Change in NE deformation during cycles 1 to 4 (n = 15 cells). Each data point under the bin of a cycle represents an individual cell in this cycle. Relative deformation was calculated relative to the deformation of cycle 1 (error bars represent SD, data were collected from 15 different cells and analyzed by one-way ANOVA, and posttest for trend, ****$P < 0.0001$). (*E*) Change in nuclear effective elastic modulus during cycles 1 to 4 (n = 15 cells). Each data point under the bin of a cycle represents an individual cell in this cycle. Relative effective elastic modulus (Relative E) was calculated relative to the effective elastic modulus of cycle 1 (error bars represent SD, data were collected from 15 different cells and analyzed by one-way ANOVA, and posttest for trend, ****$P < 0.0001$). A detailed compilation of the dataset, consisting of the comprehensive list of bead displacement measurements and the corresponding fitting of the data to the viscoelastic model, can be found in *SI Appendix*, Fig. S8.

model. The mean relative effective elastic modulus of each cycle exhibited a statistically significant trend of increase (cycle 1: 1, cycle 2: 1.11 ± 0.10, cycle 3: 1.12 ± 0.08, cycle 4: 1.18 ± 0.13; posttest for trend, $^{****}P < 0.0001$), indicating a stiffening process of the cell nucleus within seconds of the force application (Fig. 2*E*).

Nuclear Stiffening Occurs Simultaneously with Unfolding of NE Wrinkles. The cell nucleus underwent stiffening together with the unfolding of NE wrinkles (Movie S2). To analyze the unfolding of NE wrinkles, a curvature-based metric was used to quantify the structural alteration (Fig. 3*A* and *SI Appendix*, Fig. S9). Two parameters, average curvature ($\overline{\kappa}$) and average absolute curvature ($\overline{|\kappa|}$), were defined based on the curvature (κ) of a point in a planar curve to quantify the level of nuclear wrinkles inside and outside the indentation site, respectively. The indentation site is defined as the region of maximum projection of the magnetic bead's motion path on the NE, which is indicated by the black dotted lines (Fig. 3*A*). When examining a cell nucleus, a decrease in $\overline{\kappa}$ indicates that the applied force causes bending, unfolding, and stretching of the NE at the indentation site, and as a result, the NE curve transitions from a convex shape to a concave shape. On the other hand, a decrease in $\overline{|\kappa|}$ reflects the stretching and the unfolding of NE wrinkles outside the indentation site, and as a result, the NE curve becomes less deviated from being a straight line.

The in situ measurement technique is capable of simultaneously monitoring structural alteration (i.e., curvature change) and quantifying mechanical properties at the indentation site. The NE of all the measured nuclei (n = 10 cells) showed an irreversible structural alteration at the indentation site and outside the indentation site. Before the precycle, there was no force applied and the $\overline{\kappa}$ value of the cell nucleus at the indentation site was 0.08 μm^{-1} (Fig. 3*B*). In each subsequent cycle, $\overline{\kappa}$ decreased (cycle 1: 0.05 μm^{-1}, cycle 2: −0.10 μm^{-1}, cycle 3: −0.16 μm^{-1}, cycle 4: −0.18 μm^{-1}). The $\overline{|\kappa|}$ value decreased from 0.46 to 0.33 μm^{-1} after the cyclic force application (Fig. 3*C*). By comparing $\overline{\kappa}$ and $\overline{|\kappa|}$ right before the start of each cycle (Fig. 3 *D* and *E*), a significant trend of decrease was found (posttest for trend, $\overline{\kappa}$, $^{****}P < 0.0001$; $\overline{|\kappa|}$, $^{***}P = 0.0005$).

The irreversible deformation started to appear at the precycle, and each subsequent force cycle generated an additional irreversible deformation (Fig. 3*F*). Irreversible deformations were also observed when a lower cyclic force (1 nN) was applied to the cell nucleus.

To explore the relationship between the unfolding of NE wrinkles and nuclear stiffening at the indentation site, the $\overline{\kappa}$ of the NE was recorded throughout all cycles and the amount of $\overline{\kappa}$ decrease from cycle 1 to cycle 4 for each cell nucleus and the stiffening ratio were quantified. The amount of $\overline{\kappa}$ decrease from cycle 1 to cycle 4 indicates the extent of the unfolding of NE wrinkles. The stiffening ratio is the fold change of the effective elastic modulus between cycle 1 and cycle 4, which reflects the ability of a cell nucleus to stiffen under forces. A stiffening ratio higher than 1 means the stiffness increases between cycle 1 and cycle 4. It was found that the nuclei with a higher decrease in $\overline{\kappa}$ tended to have a higher stiffening ratio (Fig. 3*G*). The colormap of $\overline{\kappa}$ at cycle 1 (initial $\overline{\kappa}$) (Fig. 3*G*) and 3D visualization of the relationship between initial $\overline{\kappa}$, decrease of $\overline{\kappa}$, and stiffening ratio (*SI Appendix*, Fig. S10) show that these three variables are positively correlated. For example, the cell nucleus with the stiffening ratio of 1.06 showed almost no unfolding of NE wrinkles, as evidenced by nearly no decrease in $\overline{\kappa}$ (0.01 μm^{-1}). In contrast, the cell nucleus with the stiffening ratio of 1.49 showed significant unfolding of NE wrinkles, as evidenced by a marked decrease in $\overline{\kappa}$ (0.42 μm^{-1}). This suggests that a decrease in $\overline{\kappa}$, which occurred simultaneously with nuclear stiffening, can be a structural factor contributing to nuclear stiffening.

The monitoring of nuclear morphology was also performed after applying force of 10 nN (*SI Appendix*, Fig. S11). Three morphological parameters, namely nuclear volume, nuclear surface area, and elongation were quantified at different time points including before indentation and 10 min, 20 min, and 30 min after indentation. The results showed no significant difference between the force applied group and the control group in these morphological parameters of the nucleus at these time points.

Structural Alteration Increases Nuclear Stiffness. To further understand the contribution of NE wrinkles unfolding to nuclear stiffening, a numerical simulation was conducted, which involved the purely passive process of structural unfolding. An axisymmetric three-dimensional model was established to investigate the relationship between $\overline{\kappa}$ and stiffness. A curve was extracted from the NE wrinkles, which was then simplified to a circular arch with a varying radius denoted by R (Fig. 4*A*). The radius R was chosen to be variable to capture variations in the curvature of the local curve of the NE wrinkles. A smaller R represents a more wrinkled local NE structure, and a larger R represents a smoother local NE structure. $\overline{\kappa}$ equaling $1/R$ (see *Materials and Methods* for details of the model) decreased from 0.5 to −0.5 μm^{-1} (Fig. 4*B*), recapturing the process of unfolding shown in the in situ measurement. In the simulation, a constant force was applied to the bead for 3 s and then removed. The deformation was monitored during force application (Fig. 4*C*). Due to viscoelasticity, the deformation of the NE in the simulation showed an immediate elastic response followed by a viscous flow. Data were interpreted with the anti-Zener viscoelastic model. The results showed that with the decrease of $\overline{\kappa}$, a stiffening process occurred.

To visualize the stiffening process caused by the unfolding of the local curve of the NE wrinkles, maximum deformations of curves with different average curvatures ($\overline{\kappa}$ ranging from 0.5 to −0.5 μm^{-1}) were plotted, (Fig. 4*D*). With the decrease of $\overline{\kappa}$, deformation decreased (Fig. 4 *E* and *F*), and accordingly, the stiffness increased (Fig. 4*G*). Compared to the deformation observed at $\overline{\kappa}$ of 0.5 μm^{-1}, a significant decrease of 59% in deformation was observed at $\overline{\kappa}$ of −0.5 μm^{-1}, accompanied by an increase in the effective elastic modulus of 2.3 times. The stress and strain levels during force application under different $\overline{\kappa}$ were also analyzed (*SI Appendix*, Fig. S12). With the decrease of $\overline{\kappa}$, the maximum stress and strain all decreased markedly. Compared to values at $\overline{\kappa}$ of 0.5 μm^{-1}, there was a reduction of 36% and 24% in the maximum stress and maximum strain at $\overline{\kappa}$ of −0.5 μm^{-1}, respectively. This result shows that the passive structural alteration under force can have a significant effect on stress and strain, with a lower $\overline{\kappa}$ resulting in a substantial reduction in stress and strain. The finite element simulation suggests that the unfolding of NE wrinkles (decrease of $\overline{\kappa}$) can contribute to nuclear stiffening. Additionally, the decrease in stress and strain levels indicates that NE wrinkles serve as a load-bearing element for protecting the integrity of the cell nucleus against forces through unfolding.

Discussion

In situ measurement showed that the cell nucleus responded to forces by NE wrinkles unfolding and instantaneous stiffening. As the amount of unfolding decreased, represented by a decrease in reduced $\overline{\kappa}$, the stiffening ratio also decreased. A stiffening ratio

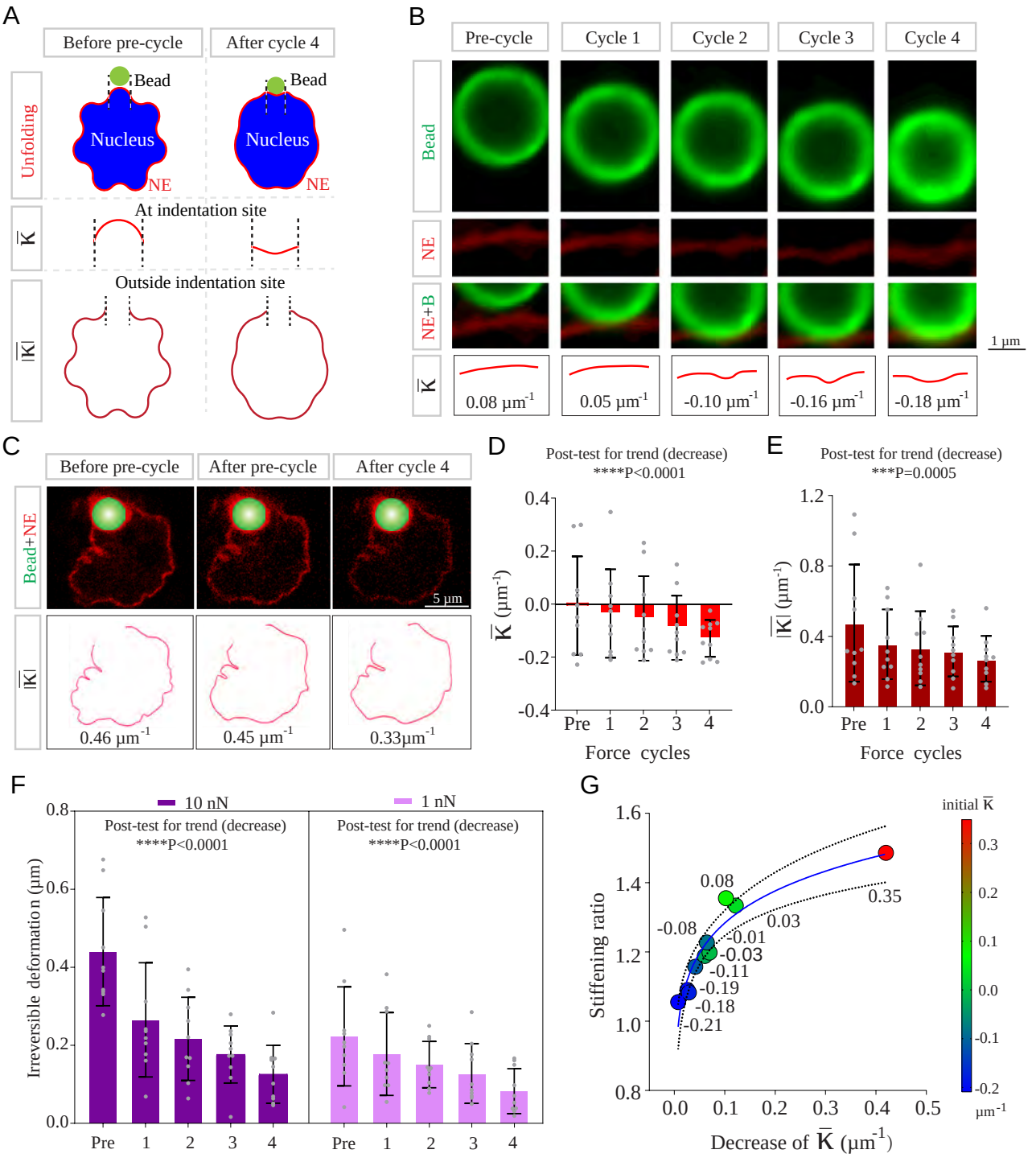

Fig. 3. Unfolding of the NE wrinkles and concurrent nuclear stiffening under force. (*A*) Schematic of the unfolding of NE wrinkles under force and curvature-based metric for quantification of NE wrinkles. Average curvature $\overline{\kappa}$ was used to quantify the curve on the NE at the indentation site (between dotted lines). Average absolute curvature $\overline{|\kappa|}$ was used to quantify the curve on the NE outside the indentation site. In a given cell nucleus, a decrease in $\overline{\kappa}$ reflects bending, unfolding and stretching of the NE that occurs at the indentation site in response to an applied force, and a decrease in $\overline{|\kappa|}$ reflects the stretching and unfolding of the NE outside the indentation site. (*B*) Confocal images of the magnetic bead and NE at the indentation site before each cycle. In this measurement, the $\overline{\kappa}$ value decreased from 0.08 μm^{-1} to −0.18 μm^{-1} during the cyclic force application. (*C*) Confocal images of NE wrinkles outside the indentation site during cyclic force application. The unfolding of NE wrinkles outside the indentation site was visualized and indicated by a decrease in $\overline{|\kappa|}$ in the middle plane of the magnetic bead. (*D*) $\overline{\kappa}$ decreased after each cycle. Each data point under the bin of a cycle represents $\overline{\kappa}$ of an individual cell right before this cycle. (n = 10 cells, error bars represent SD, data were collected from 10 different cells and analyzed by one-way ANOVA, and posttest for trend, ****$P < 0.0001$). (*E*) $\overline{|\kappa|}$ decreased after each cycle. Each data point under the bin of a cycle represents $\overline{|\kappa|}$ of an individual cell right before the cycle. (n = 10 cells, error bars represent SD, data were collected from 10 different cells and analyzed by one-way ANOVA, and posttest for trend, ***$P = 0.0005$). (*F*) At indentation forces of both 10 nN and 1 nN, irreversible deformation started to appear at precycle, and each subsequent force cycle generated an additional irreversible deformation. Totally 20 cells were measured (10 cells per force level). (*G*) Scatter plot of stiffening ratio and decrease of $\overline{\kappa}$ from cycle 1 to cycle 4. The stiffening ratio is the fold change of the effective elastic modulus between cycle 1 and cycle 4. Each data point represents an individual cell during the measurement. The cell nucleus with a higher decrease in $\overline{\kappa}$ had a higher stiffening ratio. $\overline{\kappa}$ at cycle 1 (initial $\overline{\kappa}$) is mapped to the color of data points, and each initial $\overline{\kappa}$ is also marked next to each data point (n = 10 cells, data were collected from 10 different cells and analyzed by nonlinear regression, the dotted line represents 95% confidence bands of the best-fit line). 3D visualization of the relationship between these three variables, initial $\overline{\kappa}$, decrease of $\overline{\kappa}$, and stiffening ratio, is shown in *SI Appendix*, Fig. S10.

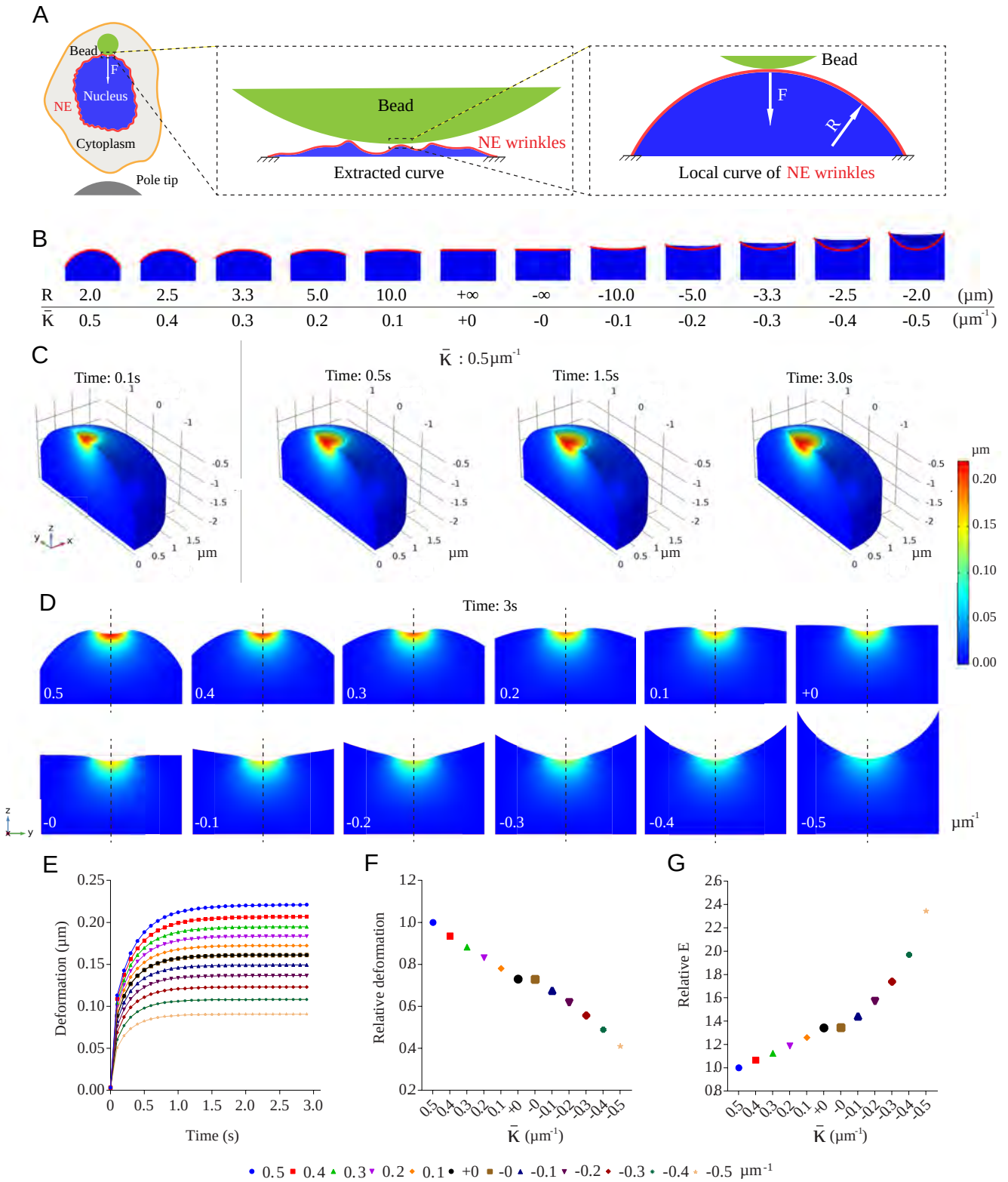

Fig. 4. Structural alteration increases nuclear stiffness (finite element method (FEM) simulation). (*A*) Schematic of the bead-curve model. A local curve from the NE wrinkles was extracted and simplified to circular arches with a radius R. Then the $\bar{\kappa}$ equals 1/R. (*B*) A sweep of $\bar{\kappa}$ from 0.5 μm^{-1} to −0.5 μm^{-1} is shown. +0 is the arch with *R* of positive infinity and −0 is the arch with *R* of negative infinity. (*C–E*) Deformation during the force application (a force equivalent to 10 nN that is used in the intracellular experiments was applied, determination of force used in the simulation is explained in the *Materials and Methods*) in the simulation (*C* and *D* shared the same scale bar). The selected time frame with the $\bar{\kappa}$ of 0.5 μm^{-1} is shown in (*C*). Maximum deformation of the curve with different $\bar{\kappa}$ under the same constant force of 3 s is shown in (*D*). In (*E*), deformation during the force application is presented. (*E*) shared the same legend for $\bar{\kappa}$ with *F* and *G*. (*F*) Deformation decreased with the reduction of $\bar{\kappa}$. Deformation data are presented as relative deformation, calculated as the deformation under a $\bar{\kappa}$ divided by the deformation under the $\bar{\kappa}$ of 0.5 μm^{-1}. (*G*) Stiffness increased with the reduction of the $\bar{\kappa}$. The data were analyzed using the anti-Zener viscoelastic model, where the variable *E* denotes the effective elastic modulus. The model and calculation of parameters are described in *Materials and Methods* and *SI Appendix*, Fig. S4. Stiffness data are presented as relative effective elastic modulus (Relative *E*), calculated as the effective elastic modulus under a $\bar{\kappa}$ divided by the effective elastic modulus under the $\bar{\kappa}$ of 0.5 μm^{-1}.

close to 1 was observed when the extent of unfolding was not apparent, which suggests the significant role of structural alteration in nuclear stiffening. Furthermore, the NE wrinkles exhibited unfolding throughout the nucleus, potentially also altering the nuclear stiffness outside the indentation site. Additionally, the finite element simulation result showed that structural alteration alone, as a purely passive process, can lead to nuclear stiffening.

Cell nuclei must adapt and react to internal and external forces in a dynamic tissue microenvironment (40) to maintain normal cellular functions (1, 2, 41, 42). It was shown that the cell nucleus can sense and respond to spatial constraints (35, 36). Here, we showed that the structural alteration of NE also contributes to nuclear stiffening. Our data, along with previous studies on the general theory of wrinkling (37, 38) on thin sheets, support curvature-induced stiffening, where the NE's wrinkling structure helps the cell nucleus withstand significant deformations via unfolding.

Wrinkled structures are ubiquitous on curved biological surfaces (27). They enable the cell membrane to expand and contract under chemotaxis (43, 44). Our results suggest that the wrinkles on curved biological surfaces also play a role in protecting structural integrity by preventing extensive deformation that can lead to NE rupture and DNA damage (1, 2). The FEM simulation results showed that NE wrinkles can reduce the level of stress and strain through unfolding. Based on the microscopic observation that applied forces flatten and smooth the NE throughout the entire cell nucleus, rather than just at the indentation site, we suspect that NE wrinkles may absorb the force and utilize the energy to alter its structure in preparation for forces that will potentially cause extensive deformation subsequently. These findings are consistent with the concept that the NE functions as an "energy sink" or "shock absorber" (33, 45) that protects nuclear integrity.

The level of deformation under cyclic force observed in this study (~2 μm) is comparable to the deformation experienced by cell nuclei during cell migration (41, 46, 47) when cells squeeze through narrow interstitial spaces in vivo that are substantially smaller than the size of the cell (48). Additionally, the folding and unfolding of NE wrinkles were also observed when cell contractility was perturbed (33) and during the transition between attachment to detachment of cells from a substrate (34).

In summary, the experimental and simulation results provide a perspective on how the cell nucleus adapts to mechanical stimuli through structural alteration of the NE wrinkles. Besides the unfolding of NE wrinkles, other active cellular processes such as the recruitment of lamin filaments (7), reorganization of chromatin (26), and force-sensitive protein–protein interactions (49, 50) may also occur upon indentation. It is likely that the structural alteration and these active processes together contribute to nuclear stiffening. Further study may decouple the contribution of other factors, providing a more comprehensive understanding of nuclear stiffening, together empowering the cell nucleus to protect its integrity and genome stability.

Materials and Methods

Single-Pole Magnetic Tweezers. To generate a large magnetic field gradient, the magnetic pole was made of HIPERCO® 50A (ASTM A801 Alloy Type 1, MIL A 47182; Carpenter Technologies Inc.), which is an iron–cobalt–vanadium soft magnetic alloy possessing high magnetic saturation (24 kG), high Direct current (DC) maximum permeability and low DC coercive force. The magnetic pole was fabricated to be 6 mm in diameter and 100 mm in length. One end of the pole was sharpened to an angle of 30°. The pole was polished and ground after heat treatment (annealing) to reach the maximum permeability of the material. To induce a magnetic gradient, a current was applied to a solenoid made of copper wire (24AWG) wrapped 544 times around the pole using 3D-printed support. The support was customized with a water-cooling system to dissipate the heat generated by the solenoid during the experiment. The solenoid was connected to a programmable DC power supply (Keithley 2260B-30-36) to generate a controllable magnetic field. The pole was mounted on a three-axis micromanipulator (MP-285; Sutter Instruments).

Magnetic Field Simulation and Force Calibration. Magnetic field simulation was performed in COMSOL Multiphysics 6.0 (COMSOL Inc.). The B-H Curve of HIPERCO® 50A was imported into the software and assigned to the pole. All simulation parameters (geometry, materials, and coil) are set the same as the real device. A sweep function from 0.5 to 2 A with a step size of 0.5 A was performed in the simulation to calculate the magnetic field under different currents. A partial differential equation was used to calculate the magnetic field gradient and force applied to the magnetic bead. Magnetic beads (Dynabeads M-270 Streptavidin; Invitrogen) were dispersed in glycerol (Sigma-Aldrich Inc.) of known viscosity (η). To avoid bead aggregation, 10 μL of beads were added to 1 mL of glycerol and sonicated (model 505; Fisherbrand). After placing the pole tip inside the bead–glycerol solution, wait for 10 min until all flows in the solution were settled. Then, the single-pole magnetic tweezers system was activated, and the movements of beads were recorded (30 FPS). Beads tracking and calculation of velocity (v) were performed by NIS-Elements AR (Nikon Inc.). The tracking algorithm was from Jaqaman, K (51). Force acting on the bead was calculated using Stokes's law $F = 6\pi\eta v$, where r is the radius of the magnetic bead (1.4 μm), and force–distance curves were generated. *SI Appendix*, Fig. S1 shows more details.

Cell Culture. Human bladder cancer T24 cells used in this study were purchased from American Type Culture Collection (ATCC). ATCC-formulated McCoy's 5A modified medium with 10% fetal bovine serum and 0.1% penicillin-streptomycin was used to culture the cells at 37 °C and 5% CO_2. The cells were passaged every 3 to 4 d using 0.05% Trypsin-EDTA (Gibco).

Transfection. Two plasmids were used in this study. pmRFP_LAP2beta_IRES_puro2b was a gift from Daniel Gerlich (Institute of Molecular Biotechnology, Dr. Bohr-Gasse 3, 1030 Vienna, Austria; Addgene plasmid #21047; http://n2t.net/addgene:21047; RRID: Addgene_21047). pBABE-puro-GFP-wt-lamin A was a gift from Tom Misteli (Center for Cancer Research, National Cancer Institute, Bethesda, MD 20892, USA; Addgene plasmid #17662; http://n2t.net/addgene:17662; RRID: Addgene_17662). Cell transfection was performed with the Lipofectamine 3000 Transfection Reagent (Invitrogen) according to the manufacturer's instructions.

Magnetic Bead Functionalization and Internalization of Beads. Atto 488 biotin (Sigma-Aldrich Inc.) was coupled to magnetic beads (Dynabeads M-270 Streptavidin; Invitrogen) through the streptavidin–biotin reaction (*SI Appendix*, Fig. S2). Then, 40 μL magnetic beads solution was placed into an Eppendorf tube. The bead solution was washed three times with Phosphate Buffered Saline (PBS) to remove preservatives. A permanent magnet was placed under the tube for 5 min to collect the magnetic beads. The beads were then resuspended in 90 μL of deionized water. Atto 488 biotin (1 mg) was diluted in 200 μL of DMSO. Then, 10 μL of this dilution was mixed with 90 μL of the magnetic bead suspension for 30 min. Finally, the solution was washed with PBS five times to remove the Atto 488 biotin surplus through magnetic separation. Lastly, the supernatant was removed, and the beads were resuspended in 40 μL of deionized water. The cells were seeded together with the functionalized magnetic beads in a Petri dish (μ-Dish 35 mm, low Grid-500; ibidi GmbH, Martinsried, Germany) on the second day after transfection. The T24 cell line is active at macropinocytosis (52). T24 cells endogenously express oncogenic Ras, which has been shown to stimulate and enhance macropinocytosis (53–55). In our experiments, the magnetic beads with a diameter of 2.8 μm were effectively internalized through macropinocytosis (*SI Appendix*, Fig. S3). In situ measurements were performed 24 h after seeding.

Live-Cell Fluorescence Imaging. A CSU-W1 spinning disk laser confocal microscope (Nikon Inc.) was used to conduct in-situ mechanical characterization and stiffening measurement experiments of the cell nucleus. An ORCA-Flash4 camera (Hamamatsu Photonics K.K.) and a 100× objective lens (CFI60 Plan Apochromat Lambda 100× Oil Immersion Objective Lens; Nikon Inc.) were used to capture images and videos during the experiment. The imaging settings for bead

displacement measurement include the following: laser source, 488 nm and 561 nm; exposure time, 100 ms per channel. A customized rotational stage was used to hold the sample during the experiments to align the bead and the cell nucleus with the direction of the force. Hoechst 33342 (Invitrogen) and CellMask plasma membrane stain (Invitrogen) were used for the live imaging of DNA and cell membrane.

Viscoelastic Model. As can be seen in Fig. 1*C*, the cell nucleus underwent both an irreversible and elastic deformation shown as an immediate elastic response followed by a slow viscous flow. Viscoelasticity of cells and cell nuclei has been widely studied using different techniques (56). Among the viscoelastic models, the anti-Zener model (57), which consists of a dashpot in series with a Kelvin–Voigt model, describes the time-dependent slow viscous flow of the cell nucleus following an immediate elastic response under a constant force condition (*SI Appendix*, Fig. S4). In the 75 fittings (5 fittings per cell, 15 cells total), the anti-Zener model had a lower root mean squared error than the Zener model (0.039 ± 0.031 vs. 0.076 ± 0.029). The anti-Zener model has also been applied to capture the viscoelastic creep behavior of cell nuclei in intact cells during micropipette aspiration (58) and isolated cell nuclei under tensile forces applied by magnetic tweezers (7). The compliance in the anti-Zener model is

$$J(t) = \frac{\varepsilon}{\sigma} = \frac{1}{E}\left(1 - e^{\left(-\frac{t}{\tau}\right)}\right) + \frac{t}{\eta_2},$$

where ε is the strain, σ is stress, η_1 and η_2 are viscosity, $\tau = \eta_1/E$ is the time constant, and E is the effective elastic modulus. The displacement of the bead in the direction of force can be related to the force by a simple relationship as shown below (6, 7, 59, 60)

$$\text{displacement}(t) = \frac{1}{6\pi r} J(t) F,$$

where r is the radius of the magnetic bead (1.4 μm), and F is the force. Original MATLAB codes (MathWorks R2022a) were utilized for curve fitting. The codes take raw data of bead displacement as input and output deformation, residual (irreversible deformation), viscosity and the effective elastic modulus (E).

Quantification of NE Wrinkles. The value of a point curvature ($|\kappa|$) is defined through the osculating circle, which is the circle that best approximates the curve at a point (x, y). $|\kappa|$ is the reciprocal of the radius of the osculating circle. $|\kappa|$ is the deviation from a straight line that a curve exhibits,

$$|\kappa| = \frac{1}{R},$$

or defined as (61)

$$|\kappa| = \frac{|\dot{x}\ddot{y} - \dot{y}\ddot{x}|}{\left(\dot{x}^2 + \dot{y}^2\right)^{\frac{3}{2}}},$$

where R is the radius of the osculating circle. In this study, the rule for the sign of the point curvature in the plane can be visualized as follows. If the center of the osculating circle is outside the cell nucleus, then the sign is positive. If the center of the osculating circle is inside the cell nucleus, then the sign is negative (*SI Appendix*, Fig. S9). The average curvature ($\overline{\kappa}$) is defined as the average point curvature of this curve. The average absolute curvature ($\overline{|\kappa|}$) is defined as the average of the absolute value of the point curvature of this curve. $\overline{\kappa}$ was used to quantify the curve on the NE inside the indentation site, which reflects the process of the NE curve transitioning from a convex shape to a concave shape. $\overline{|\kappa|}$ was used to quantify the curve on the NE outside the indentation site, which shows the amount that a NE curve deviates from being a straight line. A lower average curvature on the same cell nucleus means that the indentation site is more bent, stretched, and unfolded. A lower average absolute curvature of the same cell nucleus means that the NE outside the indentation site is more stretched and unfolded. Plugin Kappa in ImageJ was used for curvature capture (62).

Nuclear Morphology. Three morphological parameters, namely nuclear volume, nuclear surface area, and elongation were quantified using 3D imaging after staining DNA with Hoechst. Elongation (*SI Appendix*, Fig. S11*A*) characterizing the shape of the nucleus was calculated as the ratio of major and minor axis lengths. Totally 16 nuclei with magnetic beads internalized by the cells (force applied group) were monitored before applying force of 10 nN, and 10 min, 20 min, and 30 min after force application. The nuclei of another 800 cells without internalizing magnetic beads (control group) were also quantified at the same time points to establish a baseline of nuclear morphology. Statistical analysis was performed to test whether there were statistically significant differences between the control group and the force applied group (*SI Appendix*, Fig. S11 *B–D*).

Numerical Simulation. Structural mechanics simulation was performed in COMSOL Multiphysics 6.0 (COMSOL Inc.). The geometry was defined in two-dimensional under axisymmetric assumptions and revolved to form the 3D model. Structural mechanics module and a time-dependent solver were used. The bead was modeled to be a rigid body with a radius of 1.4 μm. The local curve of the NE was modeled to be viscoelastic with an elastic modulus in the range of previously studied elastic modulus of cell nucleus (1 to 10 kPa) (63), and a time constant of 0.3 s. A Poisson ratio of 0.4 (64) was assigned to the NE. To use a force equivalent to 10 nN as in the experiments, the force was calculated based on force per unit area (pressure). The area of the contact surface (assumed to be a spherical cap) was calculated based on the average deformation in all force cycles in the intracellular experiments. Then the pressure was calculated and used in the simulation. The load type in the simulation was set to force per unit area. A sweep function (from −0.5 to 0.5 μm^{-1}) was added to the simulation to alter the curvature of the local curve. To simulate one cycle in the cyclic force, a constant force was added for 3 s and then removed.

Statistical Analysis. The relative deformation, relative elastic modulus, average curvature, and stiffening ratio were reported as mean ± SD. Comparisons of each group were conducted by one-way ANOVA and posttest for trend. The *t* test was used in quantification and comparison of nuclear morphology. For each comparison, the significance level was evaluated as $*P < 0.05$, $**P < 0.01$, $***P < 0.001$, $****P < 0.0001$. GraphPad Prism was used for statistical analysis.

Data, Materials, and Software Availability. The data that support the findings of this study are included in the paper and supporting information. All original codes used in this paper are available at https://github.com/WentianTang/Viscoelastic-Model-fitting (DOI: 10.5281/zenodo.8133130) (65).

ACKNOWLEDGMENTS. This work was supported by the National Sciences and Engineering Research Council of Canada, by the Ontario Research Fund via the Research Excellence Program, and by the Canada Research Chairs Program.

Author affiliations: [a]Department of Mechanical and Industrial Engineering, University of Toronto, Toronto, ON M5S 3G8, Canada; [b]Arthur and Sonia Labatt Brain Tumour Research Centre, The Hospital for Sick Children, Toronto, ON M5G 1X8, Canada; [c]Program in Developmental and Stem Cell Biology, Research Institute, The Hospital for Sick Children, Toronto, ON M5G 1X8, Canada; [d]Department of Molecular Genetics, University of Toronto, Toronto, ON M5S 1A8, Canada; [e]Division of Orthopaedic Surgery, The Hospital for Sick Children, Toronto, ON M5G 1X8, Canada; [f]Department of Electrical and Computer Engineering, University of Toronto, Toronto, ON M5S 3G4, Canada; [g]Department of Computer Science, University of Toronto, Toronto, ON M5S 3G4, Canada; and [h]Institute of Biomedical Engineering, University of Toronto, Toronto, ON M5S 3G9, Canada

1. C. M. Denais *et al.*, Nuclear envelope rupture and repair during cancer cell migration. *Science* **352**, 353–358 (2016).
2. M. Raab *et al.*, ESCRT III repairs nuclear envelope ruptures during cell migration to limit DNA damage and cell death. *Science* **352**, 359–362 (2016).
3. J. T. Philip, K. N. Dahl, Nuclear mechanotransduction: Response of the lamina to extracellular stress with implications in aging. *J. Biomech.* **41**, 3164–3170 (2008).
4. S. Deguchi, K. Maeda, T. Ohashi, M. Sato, Flow-induced hardening of endothelial nucleus as an intracellular stress-bearing organelle. *J. Biomech.* **38**, 1751–1759 (2005).
5. J. Newberg *et al.*, Isolated nuclei stiffen in response to low intensity vibration. *J. Biomech.* **111**, 110012 (2020).
6. X. Wang *et al.*, Intracellular manipulation and measurement with multipole magnetic tweezers. *Sci. Robot.* **4**, aav6180 (2019).

7. C. Guilluy *et al.*, Isolated nuclei adapt to force and reveal a mechanotransduction pathway in the nucleus. *Nat. Cell Biol.* **16**, 376–381 (2014).
8. Y. Gruenbaum, A. Margalit, R. D. Goldman, D. K. Shumaker, K. L. Wilson, The nuclear lamina comes of age. *Nat. Rev. Mol. Cell Biol.* **6**, 21–31 (2005).
9. Y. Gruenbaum, R. Foisner, Lamins: Nuclear intermediate filament proteins with fundamental functions in nuclear mechanics and genome regulation. *Annu. Rev. Biochem.* **84**, 131–164 (2015).
10. J. Schäpe, S. Prauße, M. Radmacher, R. Stick, Influence of lamin A on the mechanical properties of amphibian oocyte nuclei measured by atomic force microscopy. *Biophys. J.* **96**, 4319–4325 (2009).
11. L. K. Srivastava, Z. Ju, A. Ghagre, A. J. Ehrlicher, Spatial distribution of lamin A/C determines nuclear stiffness and stress-mediated deformation. *J. Cell Sci.* **134**, 1–7 (2021).
12. E. A. Booth, S. T. Spagnol, T. A. Alcoser, K. N. Dahl, Nuclear stiffening and chromatin softening with progerin expression leads to an attenuated nuclear response to force. *Soft Matter* **11**, 6412–6418 (2015).
13. A. J. S. Ribeiro, P. Khanna, A. Sukumar, C. Dong, K. N. Dahl, Nuclear Stiffening Inhibits Migration of Invasive Melanoma Cells. *Cell. Mol. Bioeng.* **7**, 544–551 (2014).
14. K. Apte *et al.*, Mechanics in human fibroblasts and progeria: Lamin A mutation E145K results in stiffening of nuclei. *J. Mol. Recognit.* **30**, 1–11 (2017).
15. K. N. Dahl *et al.*, Distinct structural and mechanical properties of the nuclear lamina in Hutchinson-Gilford progeria syndrome. *Proc. Natl. Acad. Sci. U.S.A.* **103**, 10271–10276 (2006).
16. T. Dittmer, T. Misteli, The lamin protein family. *Genome Biol.* **12**, 1–14 (2011).
17. F. Alisafaei, D. S. Jokhun, G. V. Shivashankar, V. B. Shenoy, Regulation of nuclear architecture, mechanics, and nucleocytoplasmic shuttling of epigenetic factors by cell geometric constraints. *Proc. Natl. Acad. Sci. U.S.A.* **116**, 13200–13209 (2019).
18. P. M. Davidson, B. Cadot, Actin on and around the Nucleus. *Trends Cell Biol.* **31**, 211–223 (2021).
19. J. K. Kim *et al.*, Nuclear lamin A/C harnesses the perinuclear apical actin cables to protect nuclear morphology. *Nat. Commun.* **8**, 1–13 (2017).
20. W. A. Bickmore, B. Van Steensel, Genome architecture: Domain organization of interphase chromosomes. *Cell* **152**, 1270–1284 (2013).
21. M. Bustin, T. Misteli, Nongenetic functions of the genome. *Science* **352**, aad6933 (2016).
22. T. Furusawa *et al.*, Chromatin decompaction by the nucleosomal binding protein HMGN5 impairs nuclear sturdiness. *Nat. Commun.* **6**, 1–10 (2015).
23. G. Gerlitz, M. Bustin, The role of chromatin structure in cell migration. *Trends Cell Biol.* **21**, 6–11 (2011).
24. M. Krause, K. Wolf, Cancer cell migration in 3D tissue: Negotiating space by proteolysis and nuclear deformability. *Cell Adhes. Migr.* **9**, 357–366 (2015).
25. S. J. Heo *et al.*, Differentiation alters stem cell nuclear architecture, mechanics, and mechano-sensitivity. *Elife* **5**, e18207 (2016).
26. K. V. Iyer, S. Pulford, A. Mogilner, G. V. Shivashankar, Mechanical activation of cells induces chromatin remodeling preceding MKL nuclear transport. *Biophys. J.* **103**, 1416–1428 (2012).
27. Y. Tan, B. Hu, J. Song, Z. Chu, W. Wu, Bioinspired multiscale wrinkling patterns on curved substrates: An overview. *Nano-Micro Letters.* **12**, 1–42 (2020).
28. R. B. Dickinson, A. Katiyar, C. R. Dubell, T. P. Lele, Viscous shaping of the compliant cell nucleus. *APL Bioeng.* **6**, 010901 (2022).
29. I. Aifuwa *et al.*, Senescent stroma induces nuclear deformations in cancer cells via the inhibition of RhoA/ROCK/myosin II-based cytoskeletal tension. *PNAS Nexus* **2**, 1–12 (2023).
30. D. M. Jorgens *et al.*, Deep nuclear invaginations are linked to cytoskeletal filaments - integrated bioimaging of epithelial cells in 3D culture. *J. Cell Sci.* **130**, 177–189 (2017).
31. M. C. Lionetti *et al.*, Chromatin and cytoskeletal tethering determine nuclear morphology in progerin-expressing cells. *Biophys. J.* **118**, 2319–2332 (2020).
32. Y. L. Dorland *et al.*, Nuclear shape, protrusive behaviour and in vivo retention of human bone marrow mesenchymal stromal cells is controlled by Lamin-A/C expression. *Sci. Rep.* **9**, 1–15 (2019).
33. B. D. Cosgrove *et al.*, Nuclear envelope wrinkling predicts mesenchymal progenitor cell mechano-response in 2D and 3D microenvironments. *Biomaterials* **270**, 120662 (2021).
34. D. H. Kim, B. Li, F. Si, Volume regulation and shape bifurcation in the cell nucleus. *J. Cell Sci.* **128**, 3375–3385 (2015).
35. V. Venturini *et al.*, The nucleus measures shape changes for cellular proprioception to control dynamic cell behavior. *Science* **370**, eaba2644 (2020).
36. A. J. Lomakin *et al.*, The nucleus acts as a ruler tailoring cell responses to spatial constraints. *Science* **370**, eaba2894 (2020).
37. J. D. Paulsen *et al.*, Curvature-induced stiffness and the spatial variation of wavelength in wrinkled sheets. *Proc. Natl. Acad. Sci. U.S.A.* **113**, 1144–1149 (2016).
38. E. Cerda, L. Mahadevan, Geometry and physics of wrinkling. *Phys. Rev. Lett.* **90**, 4 (2003).
39. V. Pini *et al.*, How two-dimensional bending can extraordinarily stiffen thin sheets. *Sci. Rep.* **6**, 1–6 (2016).
40. M. Tanaka, M. Nakahata, P. Linke, S. Kaufmann, Stimuli-responsive hydrogels as a model of the dynamic cellular microenvironment. *Polym. J.* **52**, 861–870 (2020).
41. P. Friedl, K. Wolf, J. Lammerding, Nuclear mechanics during cell migration. *Curr. Opin. Cell Biol.* **23**, 55–64 (2011).
42. T. Harada *et al.*, Nuclear lamin stiffness is a barrier to 3D migration, but softness can limit survival. *J. Cell Biol.* **204**, 669–682 (2014).
43. L. Wang, C. E. Castro, M. C. Boyce, Growth strain-induced wrinkled membrane morphology of white blood cells. *Soft Matter* **7**, 11319–11324 (2011).
44. M. B. Hallett, C. J. Von Ruhland, S. Dewitt, Chemotaxis and the cell surface-area problem. *Nat. Rev. Mol. Cell Biol.* **9**, 662 (2008).
45. K. N. Dahl, S. M. Kahn, K. L. Wilson, D. E. Discher, The nuclear envelope lamina network has elasticity and a compressibility limit suggestive of a molecular shock absorber. *J. Cell Sci.* **117**, 4779–4786 (2004).
46. V. Te Boekhorst, L. Preziosi, P. Friedl, Plasticity of cell migration in vivo and in silico. *Annu. Rev. Cell Dev. Biol.* **32**, 491–526 (2016).
47. K. M. Yamada, M. Sixt, Mechanisms of 3D cell migration. *Nat. Rev. Mol. Cell Biol.* **20**, 738–752 (2019).
48. C. R. Hsia *et al.*, Confined migration induces heterochromatin formation and alters chromatin accessibility. *iScience* **25**, 104978 (2022).
49. Y. Tsatskis *et al.*, The NEMP family supports metazoan fertility and nuclear envelope stiffness. *Sci. Adv.* **6**, abb4591 (2020).
50. S. Na *et al.*, Rapid signal transduction in living cells is a unique feature of mechanotransduction. *Proc. Natl. Acad. Sci. U.S.A.* **105**, 6626–6631 (2008).
51. K. Jaqaman *et al.*, Robust single-particle tracking in live-cell time-lapse sequences. *Nat. Methods* **5**, 695–702 (2008).
52. C. Commisso *et al.*, Macropinocytosis of protein is an amino acid supply route in Ras-transformed cells. *Nature* **497**, 633–637 (2013).
53. D. Bar-Sagi, J. R. Feramisco, Induction of membrane ruffling and fluid-phase pinocytosis in quiescent fibroblasts by ras proteins. *Science* **233**, 1061–1068 (1986).
54. A. B. Walsh, D. Bar-Sagi, Differential activation of the Rac pathway by Ha-Ras and K-Ras. *J. Biol. Chem.* **276**, 15609–15615 (2001).
55. N. Porat-Shliom, K. Yoel, J. G. Donaldson, A unique platform for H-Ras signaling involving clathrin-independent endocytosis. *Mol. Biol. Cell* **19**, 765–775 (2008).
56. D. H. Kim, K. W. Pak, J. Park, A. Levchenko, Y. Sun, Microengineered platforms for cell mechanobiology. *Annu. Rev. Biomed. Eng.* **11**, 203–233 (2009).
57. S. Jelić, D. Zorica, Fractionalization of anti-Zener and Zener models via rheological analogy. *Acta Mech.* **234**, 313–354 (2023).
58. P. M. Davidson *et al.*, High-throughput microfluidic micropipette aspiration device to probe time-scale dependent nuclear mechanics in intact cells. *Lab Chip* **19**, 3652–3663 (2019).
59. F. Ziemann, J. Rädler, E. Sackmann, Local measurements of viscoelastic moduli of entangled actin networks using an oscillating magnetic bead micro-rheometer. *Biophys. J.* **66**, 2210–2216 (1994).
60. A. R. Bausch, W. Möller, E. Sackmann, Measurement of local viscoelasticity and forces in living cells by magnetic tweezers. *Biophys. J.* **76**, 573–579 (1999).
61. J. McCleary, *Geometry from a Differentiable Viewpoint* (Cambridge University Press, 2013).
62. H. Mary, G. J. Brouhard, Kappa (κ): Analysis of curvature in biological image data using B-splines. bioRxiv [Preprint] (2019), https://www.biorxiv.org/content/10.1101/852772v1 (Accessed 25 November 2019).
63. J. Lammerding, Mechanics of the nucleus. *Compr. Physiol.* **1**, 783–807 (2011).
64. W. R. Trickey, F. P. T. Baaijens, T. A. Laursen, L. G. Alexopoulos, F. Guilak, Determination of the Poisson's ratio of the cell: Recovery properties of chondrocytes after release from complete micropipette aspiration. *J. Biomech.* **39**, 78–87 (2006).
65. W. Tang *et al.*, Viscoelastic model fitting. *GitHub*. https://github.com/WentianTang/Viscoelastic-Model-fitting (DOI: 10.5281/zenodo.8133130). Deposited 20 June 2023.